Possible sources of the tsunami observed in the northwestern Indian Ocean following the 2013 September 24 M_w 7.7 Pakistan inland earthquake

Mohammad Heidarzadeh and Kenji Satake

Earthquake Research Institute (ERI), The University of Tokyo, Tokyo, Japan. E-mail: mheidar@eri.u-tokyo.ac.jp

SUMMARY

We report and analyse the tsunami recorded in the northwestern Indian Ocean at the Makran region following the M_w 7.7 Pakistan inland strike-slip earthquake on 2013 September 24. We analyse eleven tide gauge records as well as one DART record of this tsunami and perform numerical modelling of the tsunami that would be triggered by a range of possible sources. The tsunami registered a maximum wave height of 109 cm at the Qurayat tide gauge station (Oman). The dominant period of the tsunami was around 12 min, although wavelet analysis showed that parts of the tsunami energy were partitioned into a slightly wider period range of 7 and 16 min. Tsunami backward ray tracing showed that the tsunami source was possibly located offshore Jiwani (Pakistan) and that the tsunami was most likely triggered by the main shock. The aftershocks are distributed in the inland region and the coseismic vertical and horizontal displacements are also limited inland implying that the tsunami was generated by secondary sources triggered by the earthquake. Different possible tsunami sources including a mud volcano at the location of the newly generated island, and a mud volcano or diapir at offshore deep water were examined through numerical modelling and all failed to reproduce the observed waveforms. Numerical modelling showed that a submarine slump with a source dimension of about 10–15 km and a thickness of about 100 m located at 61.49°E and 24.62°N, that is, about 60–70 km off the Jiwani coast (Pakistan), seems capable of reasonably reproducing the wave amplitudes and periods of the observed tsunami waveforms. This event was the second instrumentally recorded tsunami in the region, after the Makran tsunami of 1945 November, and provides evidence for a hazard from landslide/slump-generated waves following seismic activity in the area.

Key words: Numerical solutions; Fourier analysis; Wavelet transform; Tsunamis; Submarine landslides; Indian Ocean.

1 INTRODUCTION

Tsunami waves were observed in the northwestern Indian Ocean following the large M_w 7.7 inland earthquake in the province of Baluchistan, southwestern Pakistan (Fig. 1). The earthquake occurred on 2013 September 24 at 11:29:47 GMT and caused a death toll of about 825 (USGS 2013a). The hypocentre of the earthquake was located at 26.971°N and 65.520°E (Fig. 1) with a depth of around 15 km. The focal mechanism showed a dominant strike slip motion (USGS 2013a). The resulting tsunami was observed along the southern coast of Iran and Pakistan, known as Makran region which hosts Makran subduction zone (MSZ; Fig. 1). This event, which we will call the Makran tsunami of 2013 hereafter, is the second instrumentally-recorded tsunami in the Makran region. The region previously experienced a large earthquake and

tsunami on 1945 November 27, leaving a death toll of around 4000 (Heidarzadeh *et al.* 2008, 2009a).

As the epicentre of the 2013 earthquake was located around 200 km inland (Fig. 1), questions were raised on how it was able to trigger the tsunami waves. The distribution of aftershocks from the first day following the event (Fig. 1) shows that the tsunami was not a direct result of earthquake crustal deformation, because no moderate or large earthquake occurred at offshore area. Satellite images before and after the earthquake showed that a new island emerged from the sea bottom due to the shakings of this large M_w 7.7 earthquake (NASA 2013). The island is located 380 km away from the epicentre in the Arabian Sea with an almost circular shape and a surface diameter of around 70–100 m (Fig. 1). The water depth at the location of this new island is around 15–20 m and it is located around 2 km from the nearest shoreline (Fig. 1). Geological
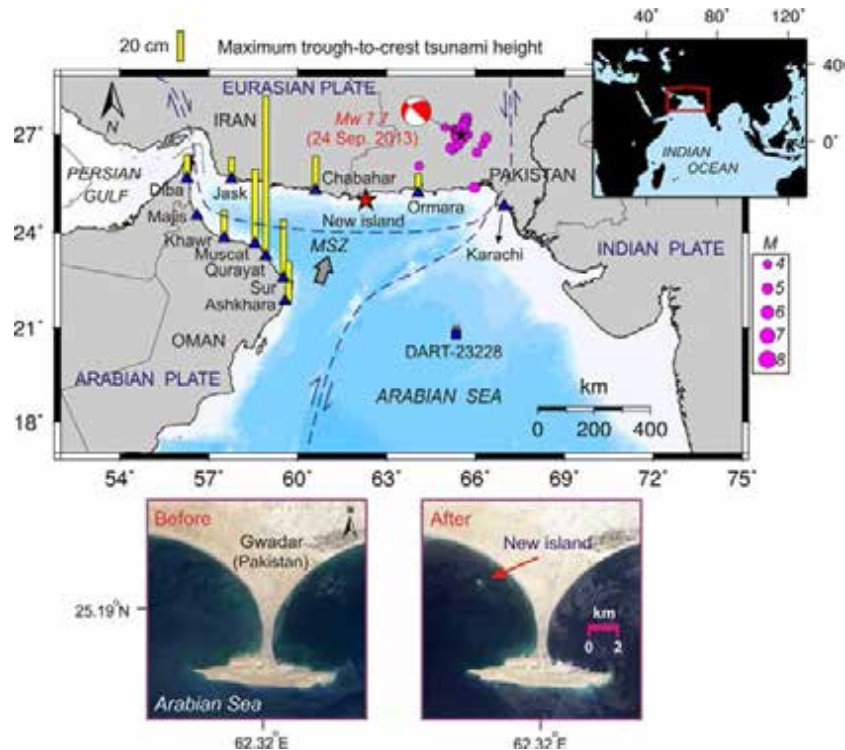
Figure 1. General map of the northwestern Indian Ocean and the epicentre of the Pakistan earthquake of 24 September 2013 earthquake (the black asterisk) along with aftershocks (M > 4.0) of the first day following the main shock, from the USGS (2013b) (solid circles). The red asterisk shows the location of the newly-generated island. The blue triangles and rectangle show the locations of the tide gauges and the DART station, respectively, whose data were used in this study. The yellow bars show maximum trough-to-crest tsunami wave heights observed at different locations. The two satellite images provided by NASA (2013) show the region before and after the earthquake indicating the birth of a new island. MSZ stands for Makran subduction zone.

surveys have shown that the island is a pile of mud and rock raised up by the earthquake shakings; possibly due to the release of gas in the layered muddy sediments (NASA 2013), that is, this new island is likely a mud volcano. The Makran region seems to be susceptible to these kinds of geological features. As an example, following the 1945 MSZ earthquake, four mud-volcano islands were created in the same region (e.g. Pendse 1946; Sondhi 1947).

The aims of this study are to characterize the observed tsunami waves in the region through analysis of the available sea level records, and to offer insights into the source of the tsunami by numerical modelling. The Makran tsunami of 2013 is of importance in several ways: first, it is the second instrumentally recorded tsunami in the Makran region; second, it was triggered by an earthquake located far inland; and third, it presents a new type of tsunami hazard for the Makran region.

2 POSSIBLE TSUNAMI SOURCES AND GEOLOGICAL BACKGROUND

A typical tsunami source is coseismic crustal deformation of which the vertical component displaces ocean water against gravity thus generating tsunami. In some cases, coseismic horizontal displacement also generates tsunamis as discussed by Tanioka & Satake (1996). To examine whether the Makran tsunami of 2013 could be the result of vertical or horizontal coseismic displacement, we calculated the coseismic crustal deformation field generated by the earthquake. We applied the analytical formulas presented by Okada (1985) which give coseismic surface deformation due to faulting in an elastic half-space. The fault parameters from seismic wave

analysis are: length 150 km, width 30 km, slip 0.5–15 m, depth 1.5–33 km, strike 216.5°, dip 44.3° and rake 388.8° (all based on USGS 2013a,c). Calculations were made using 250 subfaults; each having dimensions of 7.0 km × 5.0 km, on which we projected the finite-fault slip distribution from the USGS (2013c). Fig. 2 presents the coseismic deformation field caused by the main shock. The maximum slip on the fault surface was around 15 m (Fig. 2a). The fault motions generated maximum vertical and horizontal surface displacements of around 1 m (Figs 2b–d). It is clear from Fig. 2 that the coseismic crustal deformation field is significant only far from the nearest coastline and, thus cannot be responsible for the observed tsunami. Figs 2(c) and (d) shows that not only the vertical component, but also both components of the horizontal displacement field (Ux and Uy in Fig. 2) do not create displacements near the coast. Therefore, horizontal displacements from the main shock cannot be responsible for the observed tsunami.

As the tsunami was not generated by coseismic displacement, possibly it was triggered by submarine geological phenomena triggered by the earthquake. A review of the geological background of the region may help to obtain information about possible tsunami sources. Kukowski *et al.* (2001) performed a high-resolution bathymetric survey of the Makran region which resulted in locating previous mass wasting in the form of slumps. Bourget *et al.* (2010) presented evidence from bathymetric survey along with a reconstruction of the sedimentological history of the region, for large and recurring sliding and slumping activity in Makran. Evidence for past submarine slumping also was reported by Grando & Mc-Clay (2007), who conducted a seismic reflection survey in the region. The region also hosts many mud volcanoes and mud/shale diapirs (Delisle *et al.* 2002; Schlüter *et al.* 2002). Kassi *et al.* (2013)
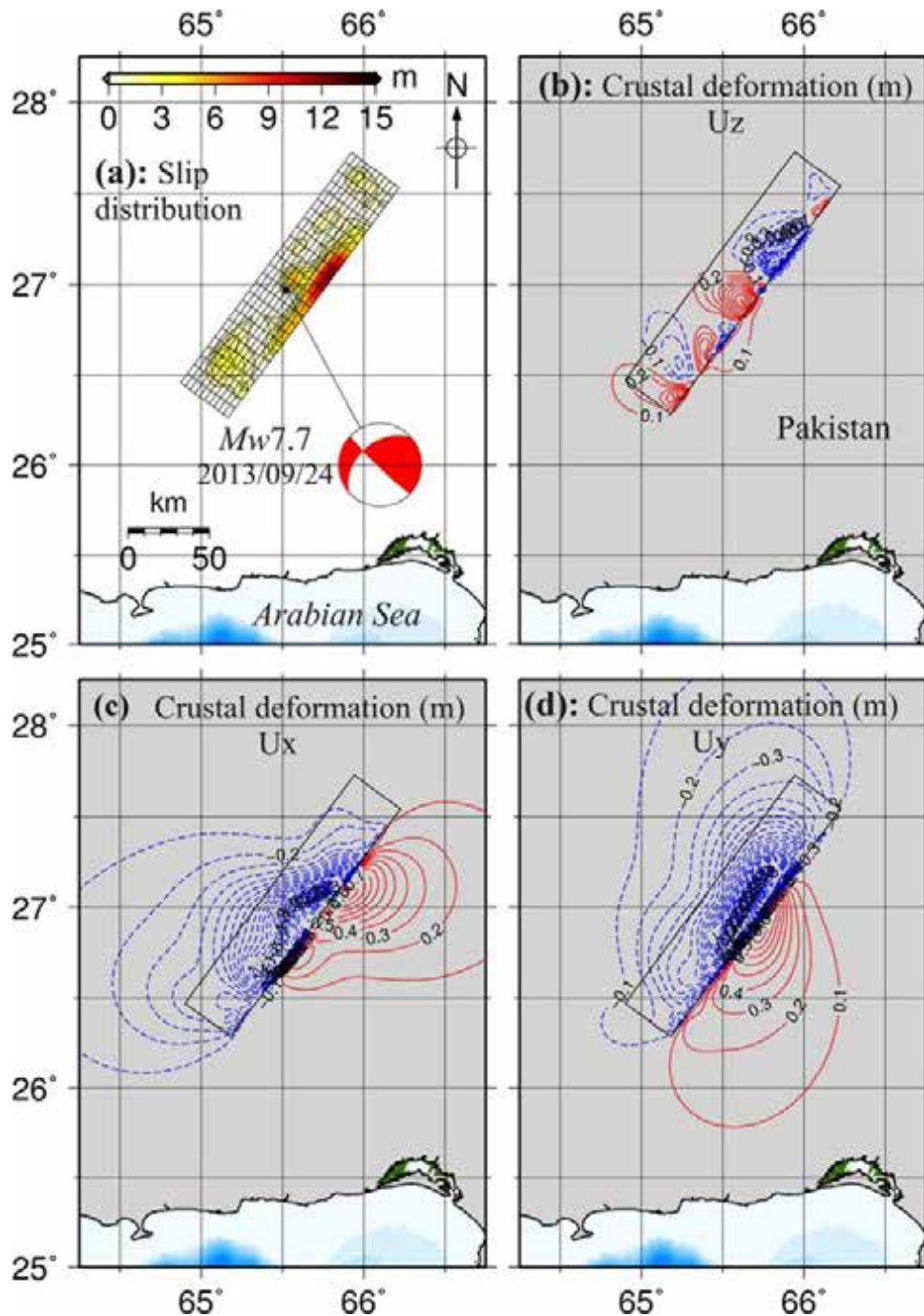
Figure 2. (a) Slip distribution of the 2013 September 24 Pakistan earthquake based on the finite fault solution of USGS (2013c). The small rectangles show 250 sub-faults used by USGS (2013c) to calculate slip distribution. (b)–(d) Surface deformation caused by the earthquake consisting of three components of: vertical displacement (Uz), east-west horizontal displacement (Ux) and north-south horizontal displacement (Uy). Rectangle delineates the fault plane.

located numerous mud volcanoes with crater diameters in the range 1–138 m both inland and offshore and warned about their possible violent extrusion due to seismic activity. Wiedicke *et al.* (2001) mapped numerous mud volcanoes with diameters mostly within 100–300 m and rarely up to around 1.5–2 km, at the water depth of around 3000 m in the Makran region.

Experience from past tsunamis has shown that most of the aforesaid phenomena can be tsunamigenic. Examples are: tsunamis from submarine landslides/slumps (e.g. 1998 July 17 Papua New Guinea tsunami; Satake & Tanioka 2003), tsunamis from mud volcanoes

(e.g. 1911 Trinidad tsunami; Lander 1997), and tsunamis from mud diapirs (e.g. 1947 New Zealand; Eiby 1982). Therefore, this short literature review shows that from a geological point of view, three candidate sources may be considered for the Makran tsunami of 2013: (1) a submarine slide/slump, (2) a mud volcano, and (3) a mud/shale diapir. Following the Makran tsunami of 2013, except for the creation of the new mud volcano island (Fig. 1), no other submarine phenomena have been reported. We examine the possibility for all these different possible sources using tsunami numerical modelling.

3 DATA

3.1 Observed tsunami

Eleven tide gauge records and one DART record of the tsunami have been collected and analysed in this study (Table 1 and Figs 1 and 3). The data come from different agencies and institutions from countries in the region (Iran, Oman, Pakistan, and India) and are made available to the scientific community by the UNESCO Intergovernmental Oceanographic Commission (IOC) and the U.S. National Oceanic and Atmospheric Administration (NOAA). All

of the analysed sea level records were digital and were sampled at 1-min intervals, but contained numerous gaps and spikes. Therefore, we processed the tsunami records to remove spikes and fill short gaps by linear interpolation. Then, we applied the tidal analysis package TASK (Tidal Analysis Software Kit) developed at the Proudman Oceanographic Laboratory (UK; Bell *et al.* 2000) for predicting and removing the tidal signal. For some of the sea level records, the tidal signal was removed by filtering since application of the TASK program was not possible due to the presence of large gaps in the data. For this purpose, the Butterworth Infinite Impulse

**Table 1.** The sea level data used in this study along with the physical properties of the observed tsunami.

No.	Type	Sea level station	Country	Longitude (°E)	Latitude (°N)	Distance[a] (km)	Arrival time[b] HH:MM (GMT)	Max wave height (cm)	Governing period (min)
1	Tide gauge record	Chabahar	Iran	60.603	25.2958	193	–[c]	23	11.6 and 40
2		Ormara	Pakistan	64.067	25.2	196	–	13.2	–
3		Sur	Oman	59.5288	22.5779	420	12:02	40	11.9
4		Qurayat	Oman	58.9251	23.2603	430	12:00	109	12.2
5		Muscat	Oman	58.5653	23.6276	449	11:59	51	12.7
6		Ashkhara	Oman	59.5732	21.8569	474	–	27	16.3
7		Jask	Iran	57.77	25.63	512	–	15	13.0
8		Karachi	Pakistan	66.975	24.811	521	–	–	–
9		Khawr Wudam	Oman	57.52	23.82	554	13:05–13:14	19	17.2
10		Majis	Oman	56.606	24.518	641	–	–	–
11		Diba	Oman	56.269	25.649	679	13:19–13:39	16	7.8
12	DART	DART-23228	India	65.347	20.799	586	12:22	1.7	7, 9, 13

[a]Distance to the location of the new island. [b]Arrival of the tsunami waves on 2013 September 24. [c]Blank items indicate that the waveform is not clear enough to let us identify tsunami arrival time or other parameters.
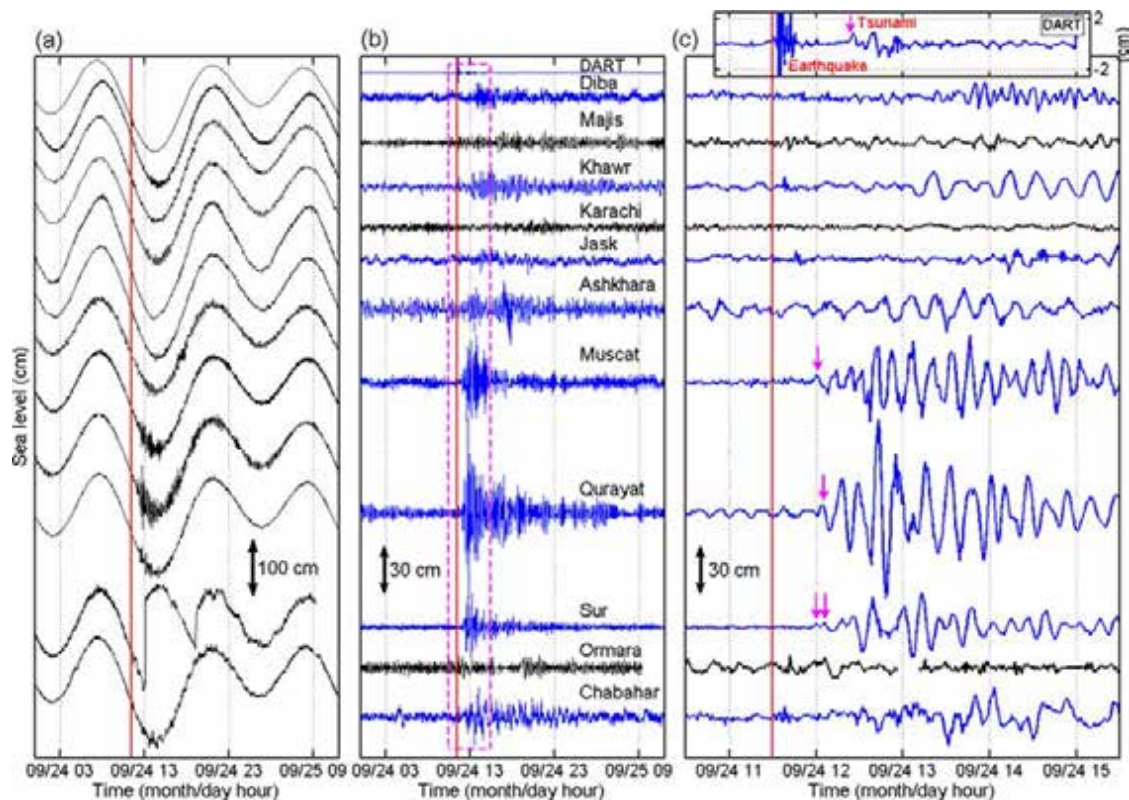

Figure 3. Tsunami waves observed in the Makran region following the M_w 7.7 Pakistan inland earthquake. (a) Original tide gauge and DART sea level records. (b) De-tided (blue waveforms) and filtered records (black waveforms). (c) Enlarged plots of the de-tided and filtered records. The dashed-purple rectangle in panel (b) shows part of the records enlarged in the panel (c). In all three panels, the first record from top belongs to the DART station. The red-vertical line represents the origin time of the main shock (i.e. 11:29:47 GMT on 2013 September 24). The purple arrows show tsunami arrival times used for tsunami backward ray tracing. For Sur, two arrows display two possible onsets; the average of the two values was used for subsequent analyses.

Bathymetry data with 8 arc-second spacing interpolated from GEBCO
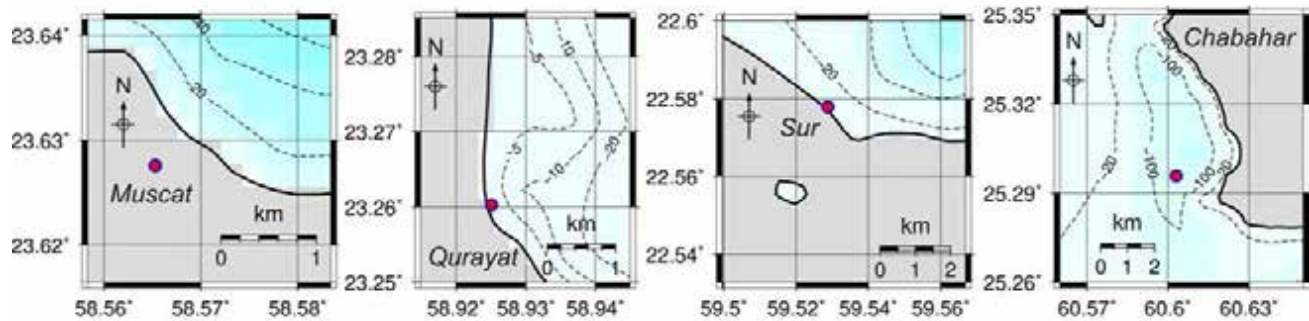
Bathymetry data with 1 arc-second spacing constructed in this study
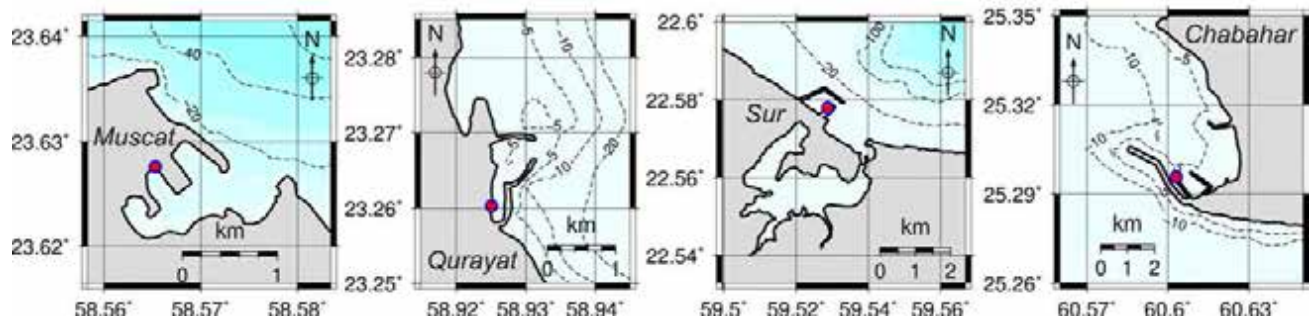
Figure 4. (Top) 8 arcsec bathymetry data for coastal sites in the region obtained by interpolating 30 arcsec bathymetry data provided by GEBCO (IOC *et al.* 2003). (Bottom) High resolution bathymetry data with grid spacing of 1 arcsec constructed in this study. Solid circles show the locations of tide gauge stations.

Response (IIR) digital filter (Mathworks 2013) was employed to remove low frequency tidal signal.

The detided waveforms are shown in Fig. 3 and their statistical characteristics are listed in Table 1. The tsunami waves are clear in most of the examined tide gauge stations. The tsunami is also clear on DART 23228 with a maximum trough-to-crest wave height of 1.7 cm (Table 1 and Fig. 3). The DART record clearly shows that a first elevation wave was recorded at this offshore station. Possibly this is the first tsunami record by this DART station, operational since 2011 October, which is among the series of DART stations deployed in the Indian Ocean in the aftermath of the 2004 December Indian Ocean tsunami. Weak and undersampled traces of seismic waves have also been recorded on this DART station. Due to the small size, the arrival time of tsunami is not clear enough in some of the examined tide-gauge records. The tsunami registered a maximum wave height of 109 cm at the Qurayat station in Oman (Figs 1 and 3). The geographical distribution of the maximum wave heights is shown in Fig. 1 indicating that most of the tsunami energy was directed towards the eastern coast of Oman in the vicinity of Qurayat and Muscat. As the location and orientation of the tsunami source are not known yet, it seems hard to attribute this observation to the directivity of tsunami waves. However, previous tsunami modelling in the region (e.g. Heidarzadeh *et al.* 2009b) showed that the bathymetric features in the region funnel part of the tsunami waves towards the eastern coast of Oman.

3.2 Bathymetry data

For the tsunami modelling, we use a combination of two different bathymetric grids: (1) the GEBCO 30 arcsec bathymetric grid (IOC *et al.* 2003) and (2) high-resolution bathymetric grid with spacing of 1 arcsec constructed in this study. The locations of some of the

tide gauge stations with relatively large wave heights are shown in Fig. 4 on the two different bathymetry grids, where the GEBCO grid has been interpolated to 8 arcsec spacing. To produce the high-resolution bathymetric grids, we combined nautical charts provided by U.S. National Geospatial-Intelligence Agency (NGA 2014) and Google-Earth satellite photos. It is clear from Fig. 4 that the GEBCO grid is not adequate to accurately account for shallow coastal bathymetric features. This is for the first time in the Makran region that such high-resolution bathymetry data is constructed and used for tsunami modelling.

4 METHODOLOGY

Our method is based on the spectral analysis of the available sea level records of this tsunami, backward tsunami ray tracing and numerical modelling of tsunami propagation from various sources. The details of these methods are explained briefly in the following.

4.1 Spectral analysis

The processed sea level records were used for spectral analysis. Tide gauges usually record a wide range of ocean signals among which are astronomical tides, various wind-generated surface waves and signals generated by local and regional bathymetric features such as harbour resonance, shelf edge waves or waves generated by refraction and reflection off bathymetric features. To distinguish signals generated by a tsunami source from other signals, Rabinovich (1997) proposed to compare spectral peaks computed from tsunami sea level data recorded at different locations, and then to pick the common spectral peaks. These common peaks most likely represent tsunami source characteristics.
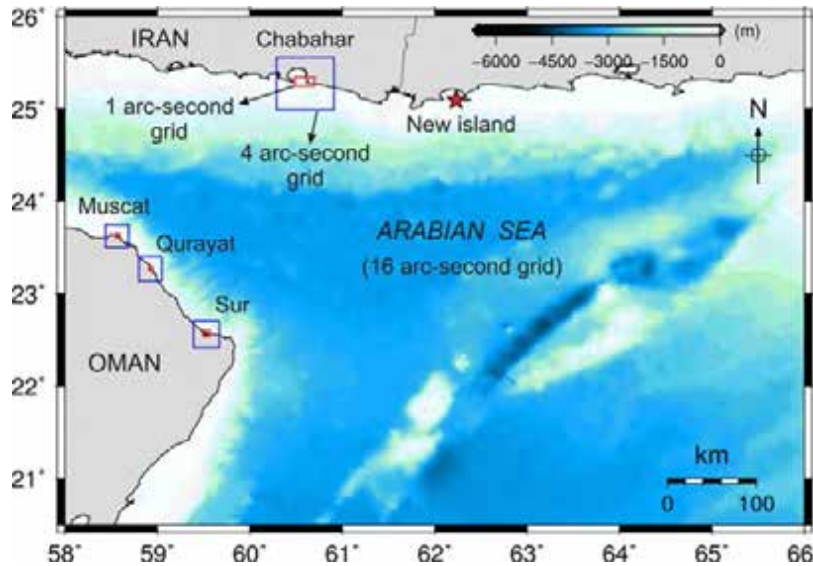
Figure 5. Map showing the three level nested grid bathymetry data with different spatial resolutions of 1 (in red boxes), 4 (in blue boxes), and 16 (elsewhere) arcsec used for tsunami modelling in this study.

We performed two types of spectral analyses: Fourier and wavelet analyses. Fourier analysis was performed using the fast Fourier transform (FFT) method for which the FFT function in Matlab program was used (Mathworks 2013). Fourier analysis is performed for both the entire tsunami waveforms whose durations are about 10 hr, and the first 2.5 hr of the waveforms. The first 2.5 hr of the waveforms may provide a better representation of the tsunami source as there is less interference of existing background signals. In addition, we performed Fourier analysis for the background signal in order to better distinguish tsunami signals from non-tsunami ones. For the wavelet analysis, we applied the wavelet package by Torrence & Compo (1998) using the *Morlet* mother function (Torrence & Compo 1998) with a wavenumber of 6 and a wavelet scale width of 0.10.

4.2 Backward tsunami ray tracing

We apply backward tsunami ray tracing to estimate the tsunami source location, using the tsunami arrival times at the different sea level stations. Backward ray tracing was performed by placing the tsunami source at each sea level station and drawing traveltime arcs corresponding to the observed tsunami traveltime to that station. For the tsunami traveltime computations, we used software TTT 3.2 (Tsunami Travel Times; Geoware 2011) which computes tsunami traveltime on actual bathymetry of the region based on the Huygen's principle (Satake 1988). A 16 arcsec bathymetry grid interpolated from the 30 arcsec bathymetric grid provided by the GEBCO digital atlas was used here (IOC *et al.* 2003). In addition, we used the 1 arcsec bathymetry grids constructed in this study for traveltime analysis within the harbours.

4.3 Tsunami numerical modelling

For modelling tsunami propagation, the well-validated numerical model COMCOT, originally developed at the Cornell University (Liu *et al.* 1998), was used. It solves the linear and non-linear shallow water equations on both Cartesian and Spherical coordinate systems using leap frog scheme on a staggered and nested grid sys-

tem (Wang 2009). A three-level nested grid system with varying grid spacing of 1, 4 and 16 arcsec is used for tsunami modelling (Fig. 5). The first level of grids with the spatial resolutions of 1 arcsec (around 30 m) was constructed in the framework of this research (Fig. 4). The other two levels of grids with grid spacing of 4 and 16 arcsec were interpolated from 30 arcsec GEBCO bathymetry (IOC *et al.* 2003). A time step of 0.75 s was applied. Tsunami inundation on dry land was not included, instead, a reflective boundary condition (also known as a vertical wall) was considered at the shoreline. At the open sea, a radiation boundary condition was imposed. Nonlinear calculations on a spherical coordinate system were performed on all grids.

Three different tsunami sources were considered: (1) mud volcanoes, (2) diapirs and (3) submarine landslides/slumps. To model tsunamis generated by mud volcanoes or diapirs, an initial uplift wave was instantaneously fed to the tsunami propagation model. For modelling landslide/slump tsunamis, three classes of modelling techniques are available (Satake 2007, 2012; Heidarzadeh *et al.* 2014). Here we apply the class of models that estimate the initial water surface at the end of the generation phase (class 2 in Heidarzadeh *et al.* 2014). This technique is based on estimating the 2-D tsunami wave height using landslide/slump source characteristics (e.g. η_{2-D}, eq. 3 in Watts *et al.* 2005; Fig. 6), and then applying empirical/analytical equations and Gaussian curve-fits to calculate the 3-D distribution of the initial tsunami wave height (i.e. η_{3-D}, eq. 5 in Watts *et al.* 1999; Fig. 6). This 3-D initial wave field is then fed to the tsunami propagation model at the end of the slide motion along with the initial velocities. It needs to be noted that the slide dimension (b in Fig. 6a) is different from the dimension of the 3-D initial wave field (L in Fig. 6b). This technique has been successfully applied to several landslide/slump tsunami cases in recent years (i.e. Synolakis *et al.* 2002; Satake & Tanioka 2003; Watts *et al.* 2003).

5 RESULTS OF SPECTRAL ANALYSIS AND TSUNAMI SOURCE DIMENSION

Results of the spectral analyses are shown in Figs 7(a) and (b). According to Fig. 7(a), most of the wave energy occurs in the period
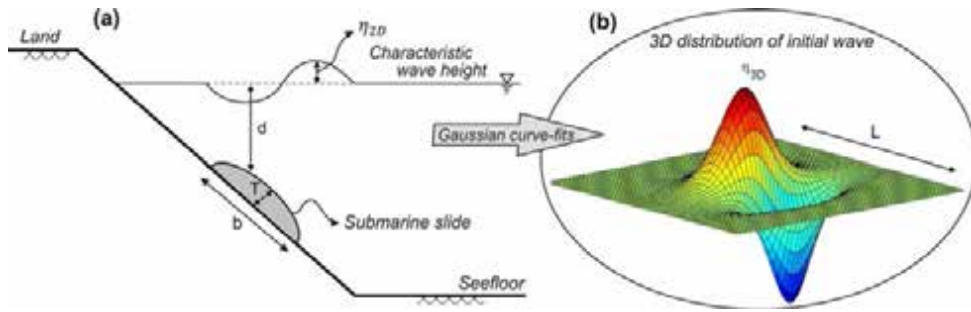
Figure 6. Sketch showing the mechanism of the second class of models used for modelling landslide/slump tsunamis according to Watts *et al.* (2005) and Heidarzadeh *et al.* (2014) (i.e. models that estimate the initial water surface at the end of the generation phase) and associated parameters.
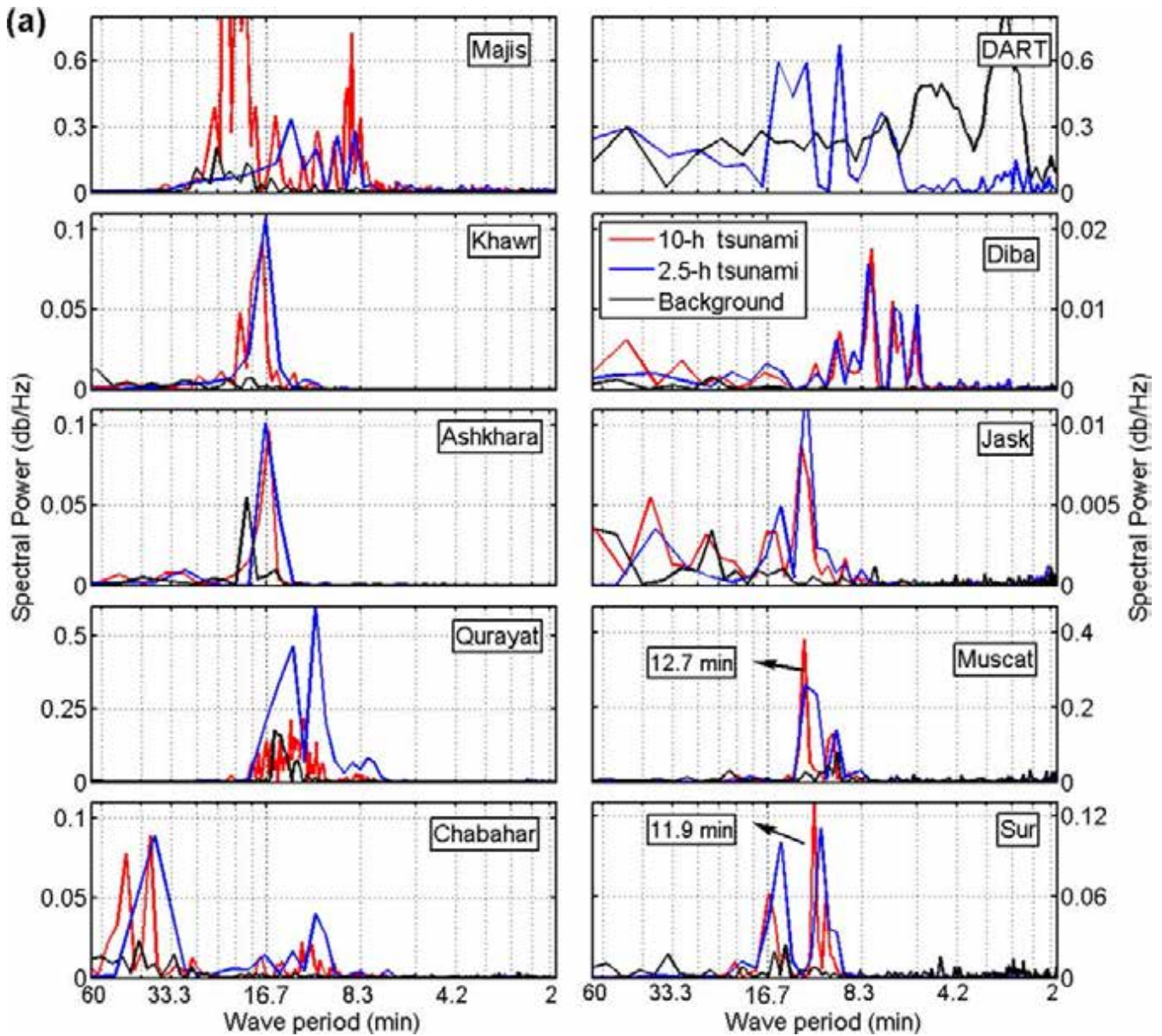

Figure 7. Spectral analysis for the waves observed in the Arabian Sea following the M_w 7.7 Pakistan inland earthquake. (a) Results of Fourier analysis. (b) Results of wavelet analysis. The color bar in wavelet plots shows Log_2 (spectral energy). GWS stands for global wavelet spectrum. The dashed line represents the origin time of the main shock (i.e. 11:29 GMT on 2013 September 24).
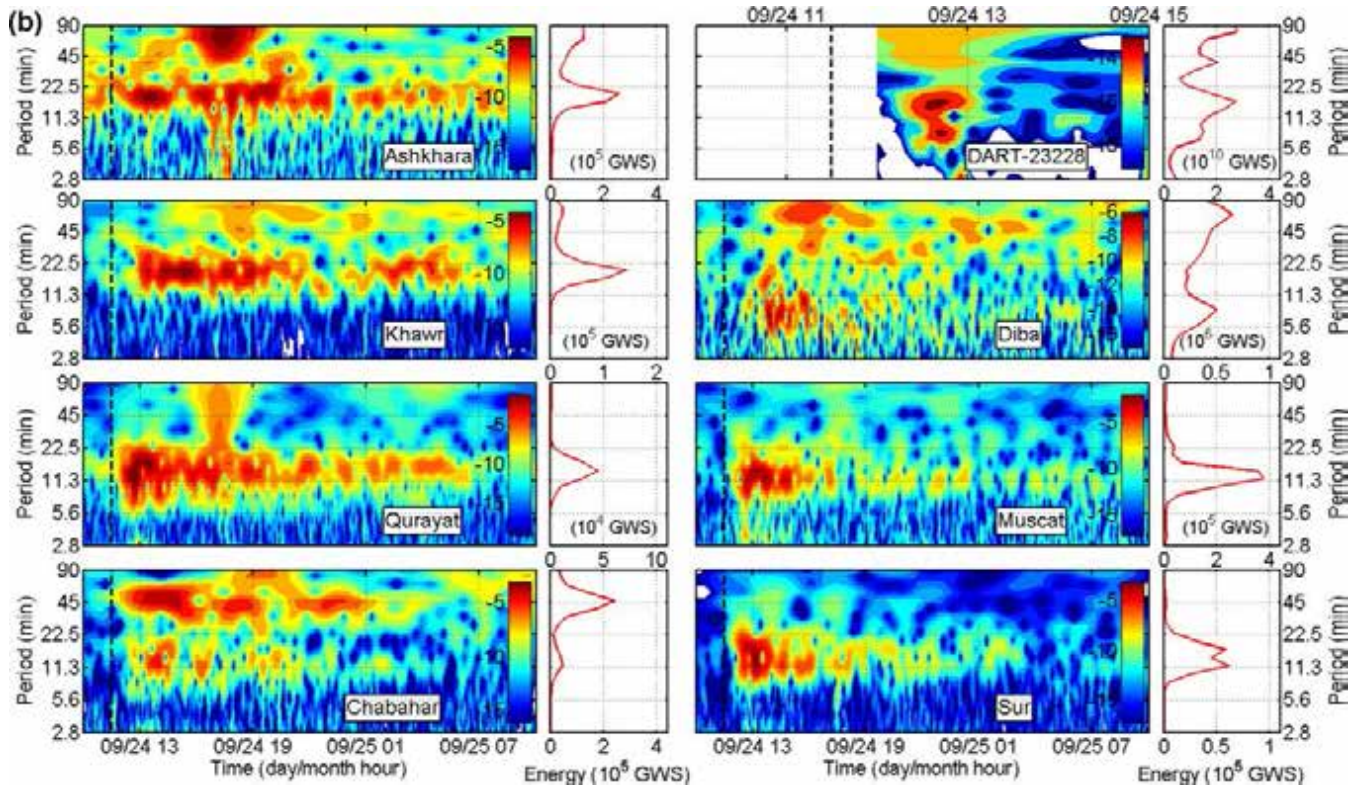
Figure 7. (*Continued.*)

range of 10–16 min, where the 12-min signal appears to be the most common dominant period. Table 1 lists the governing periods in each station. The spectra for 10- and 2.5-hr signals show similar peaks in most of the stations; however, the 2.5-hr spectra are smoother. The background signals are rather weak compared to the tsunami signals; however, their peak periods can be seen in Fig. 7(a). In some stations like Sur and Qurayat, another peak period of around 16 min is observed in both the tsunami and background spectra, suggesting the bathymetric origin of this peak. In Chabahar, the dominant period of the tsunami is about 40–45 min, though a peak period around 12 min is also clear. The background spectrum also shows a peak around 45 min in Chabahar. The tsunami spectrum for DART shows three peaks at 7, 9 and 11–14 min. As the background spectrum in this station contains a peak at 7 min (Fig. 7a), this peak also likely belongs to non-tsunami sources (e.g. bathymetric features). In summary, since the 12-min signal is most common among the examined tsunami spectra but not in the background, we may attribute it to the tsunami source.

Frequency–time (*f*–*t*) behaviour of tsunami waves from wavelet analysis are shown in Fig. 7(b). The *f*–*t* plot show that tsunami energy is switching to different period bands at different times. In some stations like Qurayat, tsunami energy is continuous in a narrow frequency band whereas in other stations like Khawr and Chabahar, some discontinuities in tsunami energy can be seen. The *f*–*t* plot for Diba shows that tsunami energy is scattered in time and frequency domains. The *f*–*t* plot for Ashkhara shows that a signal with the period of around 17 min exists in the sea level record before the occurrence of the earthquake indicating that it most likely belongs to non-tsunami sources. Similar to the Fourier analysis, wavelet results also indicate that the 12-min signal is the most common signal in different stations and possibly represents the tsunami source.
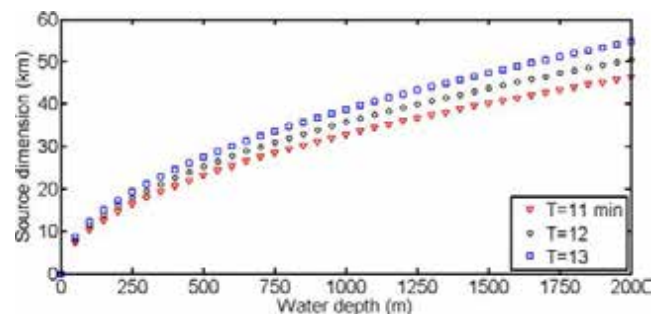
Figure 8. Simple relationship between water depth at the source and source dimension by assuming a governing period of 12 ± 1 min for the tsunami.

The dimension of the tsunami source can be roughly estimated using the results of spectral analysis by applying the tsunami phase velocity formula (Rabinovich 2009):

$$C = \sqrt{gd}, \tag{1}$$

where C is tsunami phase velocity, g is gravitational acceleration and d is water depth. By using tsunami phase velocity at the source, the tsunami source wavelength (λ) can be estimated using: $\lambda = CT$ where T is tsunami governing period. The source dimension (L) is then calculated $L = \frac{\lambda}{2}$. By assuming the tsunami governing period as 12 ± 1 min, Fig. 8 presents the expected source dimension at different water depths. According to Fig. 8, in case the tsunami occurs in the water depth of 100 m, the source dimension needs to be about 11 km to be capable of producing a governing period of 12 ± 1 min.

6 BACKWARD TSUNAMI RAY TRACING AND TSUNAMI SOURCE LOCATION

As the epicentres of the M_w 7.7 earthquake and its aftershocks were located inland, the tsunami was possibly due to a submarine phenomenon triggered by the shakings of the main shock or that of one of its aftershocks. Therefore, we assume the start time of the tsunami to be the origin time of the main shock or that of one of the aftershocks. Tsunami traveltimes according to the main shock (TTT-1 in Table 2) and the first and the largest aftershock (TTT-2 in Table 2, with magnitude M_b 5.8, occurring 6.5 min after the main shock) are listed in Table 2. Calculations of backward ray tracing were performed on a 16 arcsec grid. To investigate the effect of shallow coastal bathymetry on tsunami rays, backward ray tracing was first performed for the 1 aresec high-resolution grids at Muscat, Qurayat and Sur (Fig. 9/top). Results indicate that it takes around 2, 3 and 1 min for the tsunami waves to exit the shallow coastal areas inside the harbours in the aforesaid locations, respectively (Table 2/last column). Therefore, before applying the method on the entire Makran region with 16 arcsec grid spacing, we subtracted these corrective traveltimes from the original traveltime values.
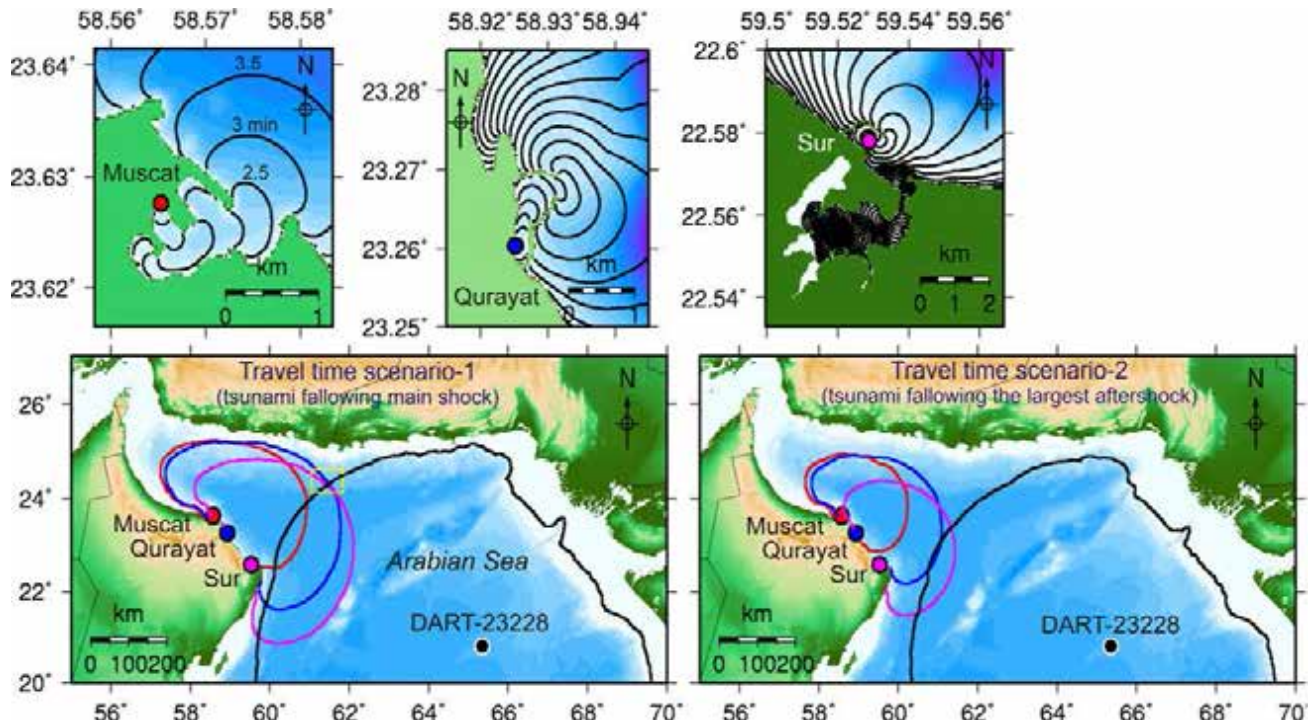
The results of backward tsunami ray tracing are shown in Fig. 9/bottom suggesting that the rays converge to an almost single zone for the scenario TTT-1 (dashed rectangle) whereas scenario TTT-2 does not converge on a single source zone. We add that the results for scenario TTT-1 is not perfect; for example, the ray originating from Muscat needs an additional time of around 5 min to arrive at the dashed zone. However, three other rays converge well to the dashed zone. The water depth of the dashed zone is around 1500–2500 m. In summary, the dashed zone in Fig. 9(bottom left-hand side) is likely to be the tsunami source zone. Another conclusion drawn from Fig. 9 is that the tsunami was most likely triggered by the main shock.

7 NUMERICAL MODELLING OF TSUNAMI PROPAGATION

As the type of the tsunami source is not clear yet, we examined three types of sources here: (1) a mud volcano at the location of the new island, (2) a mud volcano or diapir at deep water inside the

Table 2. Tsunami traveltimes by assuming different start times corresponding to the timing of the main shock or its first aftershock.

Station	Longitude (°E)	Latitude (°N)	TTT-1[a] (min)	TTT-2[b] (min)	Correction for traveltime (min)
Sur	59.520	22.570	33[c]	26.5	1
Qurayat	58.925	23.260	35	28.5	3
Muscat	58.566	23.633	31	24.5	2
DART-23228	65.347	20.799	55	48.5	0

[a]Tsunami traveltime relative to the main shock (M_w 7.7) origin time at 11:29:47 GMT on 2013 September 24.
[b]Tsunami traveltime relative to the time of the 1st and largest aftershock (Mb 5.8) at 11:36:27 GMT on 2013 September 24.
[c]This value is the average of two different traveltimes indicated by arrows in Fig. 3 for the Sur waveform.

Figure 9. (Top) Tsunami traveltime rays in the locations of Muscat, Qurayat and Sur using high-resolution bathymetry (1 arcsec grid spacing). Contour intervals are 0.5 minutes in all 3 locations. (Bottom) Results of backward tsunami ray tracing to locate the tsunami source area for two traveltime scenarios of TTT-1 (left) and TTT-2 (right) (see Table 2). The dashed rectangle in the bottom-left panel represents the potential location of the tsunami source. Solid circles represent the locations of sea level stations whose colors are the same as the ones of the respective traveltime contour lines.

Table 3. Two different mud volcano sources at the location of the new island, and a mud volcano/diapir source in deep water used for modelling of the 2013 September 24 Makran tsunami.

No.	Source type	Location		Water depth at the source (m)	Diameter (km)	Max uplift (m)
		Longitude (ºE)	Latitude (ºN)			
1	Mud volcano at new island	62.275	25.166	15–20	1.5	15
2	Mud volcano at new island	62.275	25.166	15–20	2	20
3	Mud volcano/diapir at deep water	61.499	24.406	1800	2	20

source zone predicted by backward tsunami ray tracing and (3) a submarine landslide/slump source inside the source zone.

7.1 A mud volcano at the location of the new island

We assumed the tsunami source to be located at the place of the new island emerged in the Arabian Sea following the earthquake (Fig. 1). Two mud volcano sources were modelled as conical sources with different diameters and initial heights (Table 3). Previous geological surveys have shown that the diameters of mud volcanos in the region, even in deep water, are mostly in the range 100–300 m and rarely reach extreme values of 1.5–2 km (e.g. Wiedicke *et al.* 2001). However, we apply the extreme values of 1.5 and 2 km for our modelling efforts (Table 3), as the spectral analyses indicate source dimensions on the order of kilometres to tens of kilometres (Fig. 8). Fig. 10 shows the locations and 3-D plots of these sources along with the simulation results. Results indicate that the agreement between the observed and simulated waveforms is rather poor both in terms of arrival times and wave amplitudes as well as wave periods. The simulated waves arrive 0.5–1 hr later than the observed ones in most stations. This seems evident as both of the sources are located inside an extremely shallow semi-enclosed bay. Any tsunami within this bay, first, moves rather slowly and hence rapidly loses its wave amplitudes; and second, can hardly exit the bay due to its semi-enclosed shape. Therefore, the simulations may suggest that the tsunami source was located outside of the bay in deeper water, in agreement with our tsunami backward ray tracing results (Fig. 9).

7.2 A mud volcano or diapir in deep water

As the second possibility, we model a hypothetical mud volcano or diapir located in deep water inside the source zone predicted by backward tsunami ray tracing. The study by Wiedicke *et al.* (2001) showed that mud volcanoes with diameters of up to 1.5–2 km have previously occurred around the source zone in Fig. 9. We assume that the tsunami generation mechanism for diapirs and mud volcanoes is similar to each other. For both, we consider an instantaneous initial elevation wave with diameter of 2 km and a maximum initial height of 20 m. Fig. 11 presents the result. The agreement between the observed and simulated waveforms is still poor although the arrival times are almost similar. The simulated amplitudes are smaller than the observed ones and the wave periods are too short relative to the observed waves. This simulation indicates that the true source of the 2013 Makran tsunami is likely to be located in deep water but requires a larger source dimension in order to be able to produce longer wave periods.

7.3 A submarine landslide/slump source

Based on Fig. 8, a source dimension of around 40 km is necessary to produce a governing period of around 12 min at the water depth

of 1500–2500 m. As the maximum dimension of a mud volcano can reach a value of up to 1.5–2 km (Wiedicke *et al.* 2001), a larger source is needed. Our simulations from mud volcano sources also indicate that a more powerful source is necessary to reproduce the observed waveforms. As no earthquake has been detected in the estimated tsunami source location from backward tsunami ray tracing (Fig. 9), a submarine landslide or slump seems likely to be the source of the tsunami. As discussed above, the Makran region has been shown to be susceptible to submarine sliding or slumping. We consider a submarine slump here because previous studies showed that slumping is the more likely mode of submarine mass wasting in the region (e.g. Kukowski *et al.* 2001; Bourget *et al.* 2010).

We perform a sensitivity analysis to determine an optimum slump source for the 2013 Makran tsunami. Before performing the mentioned sensitivity analysis, we conduct initial simulations using three slump scenarios with dimensions of 3, 6 and 9 km and an initial thickness of 100 m in order to obtain an initial estimate of the dimension of a slump scenario that can match with the observed waveforms (scenarios INI 1–3 in Table 4). Results are shown in Fig. 12(d) indicating that the simulated wave periods are clearly shorter than the observed ones for the two scenarios of INI-1 and INI-2. Results for the scenario INI-3 showed better agreement with observations; however, still the source dimension needs to be slightly increased. Therefore, for our sensitivity analysis, we changed source length, width and thickness in the ranges 10–20 km, 10–20 km and 75–125 m, respectively (Table 4). For all sources, the mean slope angle of the region is taken as 2º, following Kukowski *et al.* (2001), and the bulk density of material was assumed to be 2000 kg m^{-3}. The 2-D and 3-D projection of one of these sources along with the results of tsunami simulations for all scenarios are presented in Fig. 12. The root mean square errors (RMSE) of the simulations in comparison to the observation at the DART station are calculated to help us judging about the quality of fit (Table 4/last column). The RMSE criterion does not seem useful for other tide gauge records because there is a phase shift between observations and simulations at those stations. Our target for an acceptable fit is the reproduction of wave periods and amplitudes because full reproduction of arrival times and details of the observed waveforms seems difficult due to the simplified nature of our submarine slump modelling based on Watts *et al.*'s (2005) method.

The simulated wave periods and amplitudes are close to those of observations for some of the examined scenarios (e.g. scenarios T-100, W-10, W-15 and L-15 in Figs 12e–g). Both RMSEs and simulated waveforms resulting from scenarios T-100, W-10, W-15 and L-15 are close to each other. Therefore, by a visual look at the nine scenarios of length, width and height, and by taking into account the RMSE for different scenarios, we may conclude that a slump scenario with a dimension of about 10–15 km and a thickness of around 100 m can reasonably reproduce the observed wave periods and amplitudes (Fig. 12h). In Qurayat, there is time lag between the largest observed wave amplitude of 109 cm and the simulated one. The agreement between observed and simulated
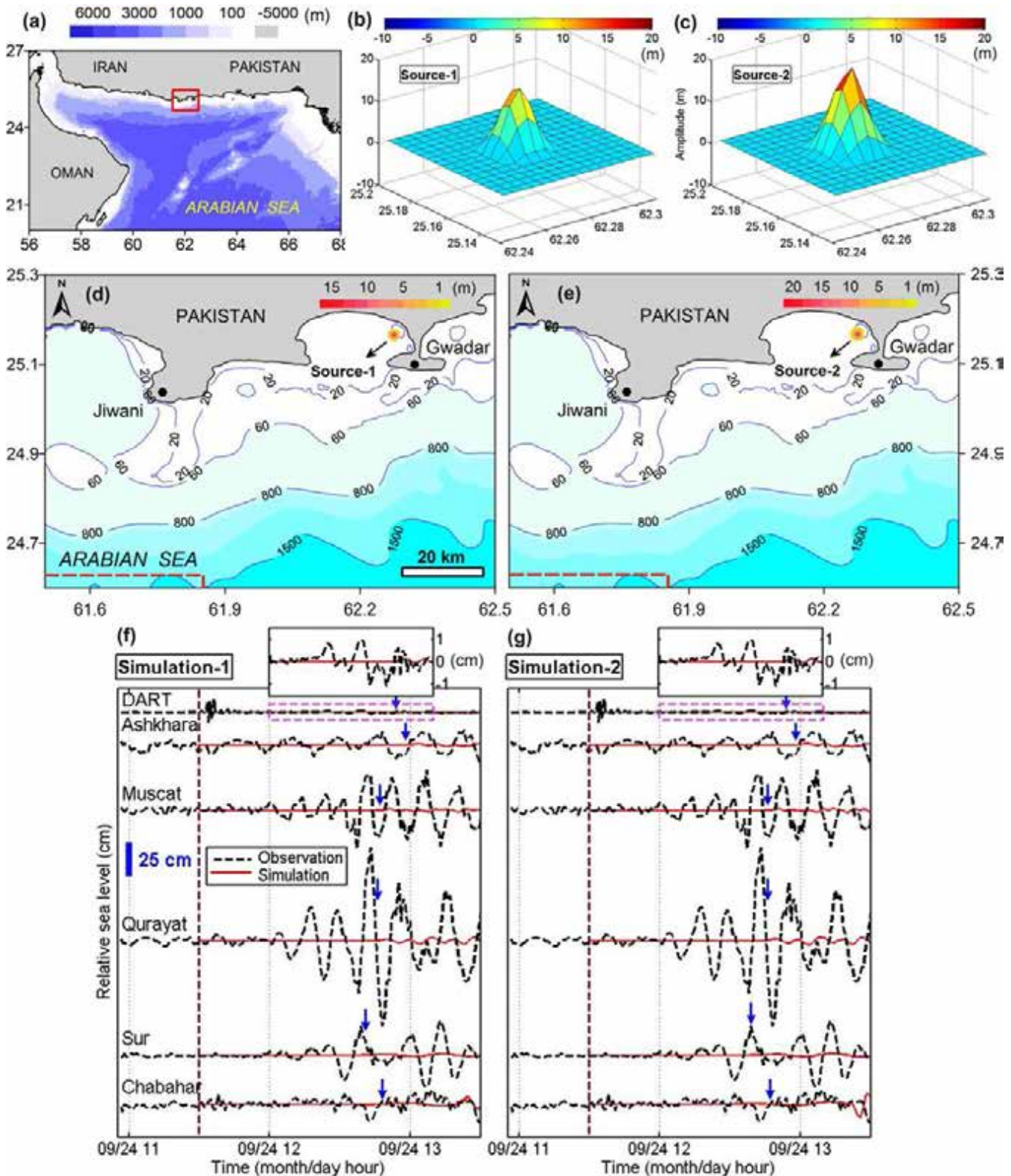
Figure 10. (a) Location of the tsunami sources at the location of the newly-generated island, within the entire Makran region. (b)–(c) 3D projections of two mud volcano tsunami sources with maximum initial uplifts of 15 and 20 m, respectively. (d)–(e) Locations of the two mud volcano tsunami sources in comparison to local bathymetry. The dashed lines show the borders of the source zone predicted by the backward ray tracing (Fig. 9). (f)–(g) Comparison of the observed (black-dashed lines) and simulated waveforms (red-solid lines) resulting from two mud volcano tsunami sources 1 and 2, respectively. The dashed-vertical line shows the origin time of the main shock. The blue arrows show the arrival times of tsunami for simulations.
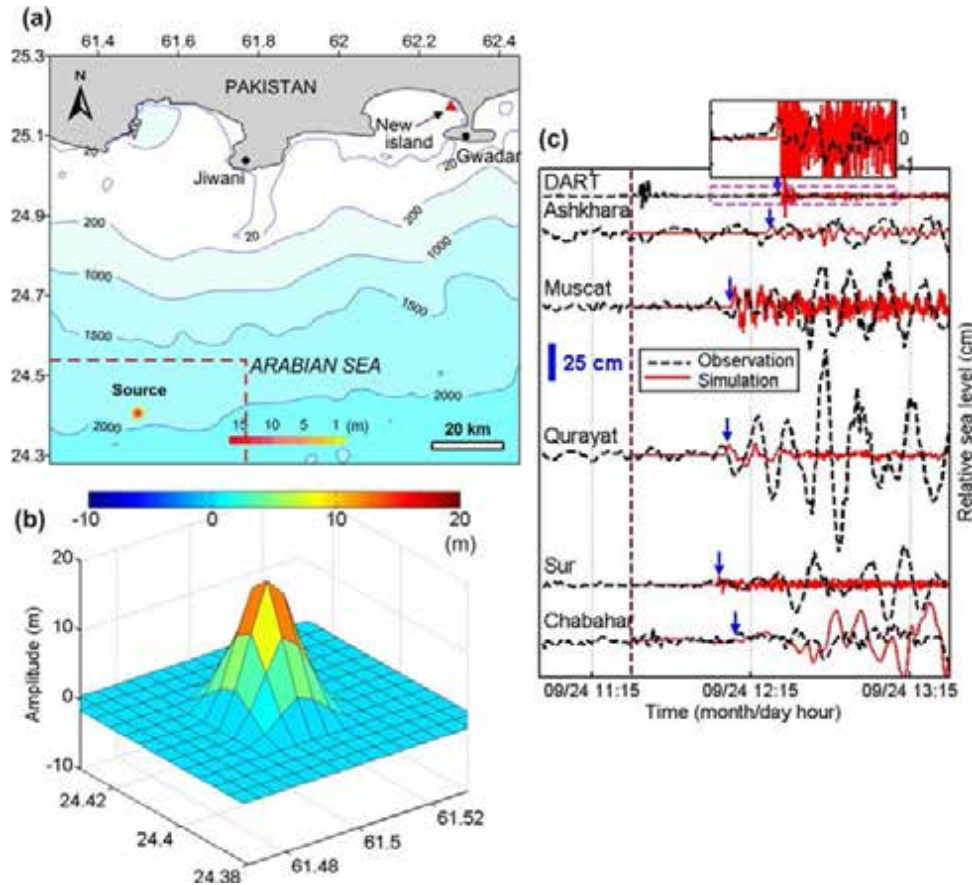
Figure 11. (a) Location of a mud volcano or diapir as a possible source of the tsunami inside the source zone predicted by tsunami backward ray tracing. The dashed lines show the borders of the source zone predicted by our backward ray tracing (Fig. 9). (b) 3D projection of the tsunami source. (c) Comparison of the observed (black-dashed lines) and simulated waveforms (red-solid lines). The blue arrows show the arrival times of tsunami for simulations.

Table 4. Details of submarine slump scenarios considered to model the 2013 September 24 Makran tsunami. The bold-italic numbers indicate parameters that change in every class of simulations.

	Source scenario name	Location Lon. (°E)	Location Lat. (°N)	b[1] (km)	W[2] (km)	T[3] (m)	D[4] (m)	TD[5] (km)	t0[6] (s)	Umax (m/s)[7]	η_{2D}[8] (m)	η_{3D}[9] (m) Max. Dep.	η_{3D}[9] (m) Max. Ele.	RMSE[10]
Initial	INI-1	61.49	24.20	3.0	3.0	100.0	2000	10.0	59.8	83.6	5.3	−5.9	4.5	–[a]
	INI-2	61.49	24.20	6.0	6.0	100.0	2000	10.0	119.3	41.9	2.4	−2.7	2.0	–
	INI-3	61.49	24.20	9.0	9.0	100.0	2000	10.0	179.0	27.9	1.5	−1.7	1.3	–
Length	L-10	61.49	24.62	*10.0*	15.0	100.0	1500	10.0	199.0	25.1	2.1	−2.9	2.2	1.10
	L-15	61.49	24.62	*15.0*	15.0	100.0	1500	10.0	298.3	16.8	1.3	−1.5	1.1	0.74
	L-20	61.49	24.62	*20.0*	15.0	100.0	1500	10.0	397.7	12.6	0.9	−0.9	0.7	0.65
Width	W-10	61.49	24.62	15.0	*10.0*	100.0	1500	10.0	298.3	16.8	1.3	−1.1	0.8	0.55
	W-15	61.49	24.62	15.0	*15.0*	100.0	1500	10.0	298.3	16.8	1.3	−1.5	1.1	0.74
	W-20	61.49	24.62	15.0	*20.0*	100.0	1500	10.0	298.3	16.8	1.3	−1.7	1.3	0.95
Height	T-075	61.49	24.62	15.0	15.0	*75.0*	1500	10.0	344.4	14.5	0.7	−0.7	0.6	0.54
	T-100	61.49	24.62	15.0	15.0	*100.0*	1500	10.0	298.3	16.8	1.3	−1.5	1.1	0.74
	T-125	61.49	24.62	15.0	15.0	*125.0*	1500	10.0	266.8	18.7	2.0	−2.5	1.9	1.08
	Final source	61.49	24.62	10–15	10–15	100.0	1500	10.0	298.3	16.8	1.3	−1.5	1.1	0.74

[1]Slump length (Fig. 6), [2]Slump width, [3]Slump thickness (Fig. 6), [4]Water Depth, [5]Travel Distance, [6]Characteristic time, [7]Maximum velocity, [8]Characteristic 2D wave height (Fig. 6), [9]Initial 3D wave height (Fig. 6), [10]Root Mean Square Misfit (RMSE) between the model and the DART record.
[a]Calculations of RMSE are not possible because the simulated waves are too short compared to the observed ones.
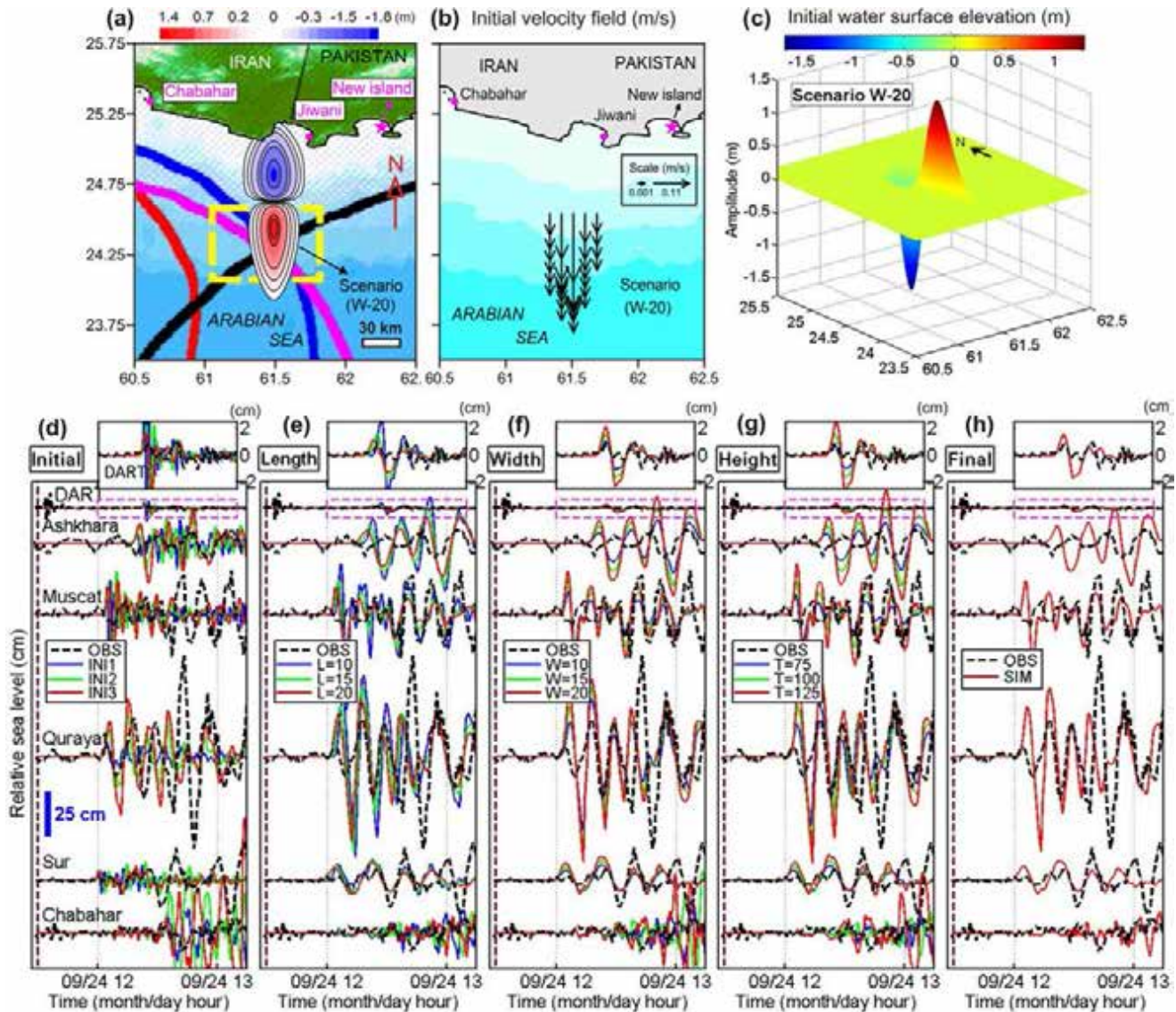
Figure 12. (a) 2D projection of the slump scenario of W-20. The dashed rectangle shows the possible tsunami source location predicted by backward ray tracing. (b) Initial tsunami velocity field used for tsunami modelling for scenario W-20. (c) 3D projection of the initial water surface elevation for slump scenario W-20. (d)–(g) Comparison of observed (black-dashed lines) and simulated (colored-solid lines) waveforms for different scenarios of slump sources. The dashed-vertical line shows the origin time of the main shock. (h) Comparison of observed (black-dashed lines) and simulated (colored-solid lines) waveforms for the final preferred slump source.

waves is generally good for the DART record. Our final source is close to the scenarios T-100, W-10, W-15 and L-15 which yield minimum RMSE among the investigated scenarios (Table 4). In summary, based on Table 4 and Fig. 12, we propose the possible landslide source parameters as: slide dimension, ~10–15 km; slide thickness, ~100 m; and location, 61.49°E, 24.62°N. This location is around 60–70 km offshore Jiwani (Pakistan) (Fig. 12).

8 DISCUSSIONS

8.1 Lack of a perfect agreement between observations and simulations

The agreement between simulated and observed waveforms (Fig. 12h) was not as good as that usually reported for tectonic tsunamis. However, this is expected because the source of tectonic

tsunamis can be considered instantaneous, whereas this assumption does not usually hold true for landslide/slump sources due to the relatively slow generation process for these tsunamis. In fact, the Watts *et al.*'s (2005) method used here for modelling landslide tsunamis is based on the approximation of the initial out-of-equilibrium water surface at the end of slump and neglects the complex slow generation of submarine mass failures. In addition, this method assumes an initial simple 3-D surface for the tsunami source whereas actual tsunami sources are heterogeneous. These assumptions are likely partly responsible for the lack of a good agreement between simulated and observed waveforms. Based on these simplifications, we would not usually expect to produce a full match between observations and simulations. Past applications of Watts *et al.*'s (2005) method for modelling submarine mass failures targeted only maximum coastal run-up heights (e.g. Synolakis *et al.* 2002; Watts *et al.* 2005). However, the application of more sophisticated models for modelling submarine slump tsunamis (e.g. Heidarzadeh *et al.*

2014) need detailed information about seafloor bathymetry and the slumping mass which are not currently available for the region.

8.2 Landslide/slump tsunami hazards in Makran

Assuming that the 2013 September 24 tsunami was generated by a submarine slump triggered by the inland earthquake, this event can be considered as evidence that the region is susceptible to submarine mass failures following seismic activity, even inland. This has been previously reported by some authors based on geological and sedimentological investigations in the region (e.g. Kukowski *et al.* 2001; Grando & McClay 2007; Bourget *et al.* 2010). It has been already speculated that the 12–15 m of run-up observed in the near-field following the 1945 November 27 earthquake (M_w 8.1) in the same region was produced by a possible local submarine mass failure triggered by the earthquake (Heidarzadeh *et al.* 2008).

9 CONCLUSIONS

We analysed the tsunami observed in the northwestern Indian Ocean following the Pakistan M_w 7.7 inland strike-slip earthquake by studying 12 sea level records and simulations of a number of potential sources through numerical modelling. Our main findings are:

1. The tsunami was clear in most of the examined sea level records, where a maximum trough-to-crest wave height of 109 cm was registered in Qurayat (Oman).

2. Calculation of coseismic deformation showed that vertical and horizontal displacement fields only reach significant values far from the coast indicating that the tsunami was not the result of vertical or horizontal coseismic displacement.

3. Analysis of the distribution of aftershocks in the first day following the main shock showed that all of them were located inland, indicating that the tsunami was generated by secondary sources triggered by the earthquake.

4. The tsunami governing period was around 12 min, although wavelet analysis showed that parts of the tsunami energy were partitioned into other period bands of 7 and 16 min. This governing period implies a source dimension of about 45 km for a source located at the water depth of 1500 m.

5. Tsunami backward ray tracing showed that: first, the tsunami source was possibly located at offshore Jiwani (Pakistan); and second, it was most likely triggered by the main shock.

6. Tsunami modelling assuming a mud volcano at the location of a new island, created in the Arabian Sea following the earthquake, was not successful in reproducing the observed sea level records.

7. Separate modelling showed that a mud volcano or diapir in deep water, at the location inferred from backward ray tracing, is not also capable of reproducing the observations. Therefore, mud volcanoes or diapirs are not likely to be a possible source for the observed tsunami.

8. A submarine slump source with a source dimension of about 10–15 km, a thickness of about 100 m located at 61.49°E and 24.62°N seems capable of reasonably reproducing the observed sea level records. This source is located about 60–70 km off the Jiwani coast (Pakistan).

REFERENCES

Bell, C., Vassie, J.M. & Woodworth, P.L., 2000. POL/PSMSL Tidal Analysis Software Kit 2000 (TASK-2000), Permanent Service for Mean Sea Level. CCMS Proudman Oceanographic Laboratory, UK.

Bourget, J. *et al.*, 2010. Highstand vs. lowstand turbidite system growth in the Makran active margin: Imprints of high-frequency external controls on sediment delivery mechanisms to deep water systems, *Mar. Geol.,* **274**(1), 187–208.

Delisle, G., Von Rad, U., Andruleit, H., Von Daniels, C., Tabrez, A. & Inam, A., 2002. Active mud volcanoes on-and offshore eastern Makran, Pakistan, *Int. J. Earth Sci.,* **91**(1), 93–110.

Eiby, G.A., 1982. Earthquakes and tsunamis in a region of diapiric folding, *Tectonophysics,* **85**(3), T1–T8.

Geoware, 2011. The Tsunami Travel Times (TTT). Available at: http://www.geoware-online.com/tsunami.html (last accessed December 2013).

Grando, G. & McClay, K., 2007. Morphotectonics domains and structural styles in the Makran accretionary prism, offshore Iran, *Sediment. Geol.,* **196**(1), 157–179.

Heidarzadeh, M., Pirooz, M.D., Zaker, N.H., Yalciner, A.C., Mokhtari, M. & Esmaeily, A., 2008. Historical tsunami in the Makran subduction zone off the southern coasts of Iran and Pakistan and results of numerical modeling, *Ocean Eng.,* **35**(8–9), 774–786.

Heidarzadeh, M., Pirooz, M.D. & Zaker, N.H., 2009a. Modeling the near-field effects of the worst-case tsunami in the Makran subduction zone, *Ocean Eng.,* **36**(5), 368–376.

Heidarzadeh, M., Pirooz, M.D., Zaker, N.H. & Yalciner, A.C., 2009b. Preliminary estimation of the tsunami hazards associated with the Makran subduction zone at the northwestern Indian Ocean, *Nat. Hazards,* **48**(2), 229–243.

Heidarzadeh, M., Krastel, S. & Yalciner, A.C., 2014. The state-of-the-art numerical models for modeling landslide tsunamis: a short review, in *Submarine Mass Movements and Their Consequences,* pp. 483–495, eds Krastel, S. *et al.*, Springer.

IOC, IHO, & BODC, 2003. Centenary edition of the GEBCO digital atlas, published on CD-ROM on behalf of the Intergovernmental Oceanographic Commission and the International Hydrographic Organization as part of the general bathymetric chart of the oceans, British Oceanographic Data Centre, Liverpool, UK.

Kassi, A.M., Khan, S.D., Bayraktar, H. & Kasi, A.K., 2013. Newly discovered mud volcanoes in the Coastal Belt of Makran, Pakistan—tectonic implications, *Arab. J. Geosci.,* doi:10.1007/s12517-013-1135-7.

Kukowski, N., Schillhorn, T., Huhn, K., von Rad, U., Husen, S. & Flueh, E.R., 2001. Morphotectonics and mechanics of the central Makran accretionary wedge off Pakistan, *Mar. Geol.,* **173**(1), 1–19.

Lander, J.F., 1997. Caribbean tsunamis: an initial history, in *Natural Hazards and Hazard Management in the Greater Caribbean and Latin America,* pp. 1–18, ed. Ahmad, R., The University of West Indies, Mona, Jamaica.

Liu, P.L.-F., Woo, S-B. & Cho, Y-S., 1998. Computer programs for tsunami propagation and inundation. Technical report, Cornell University, 111 pp.

Mathworks, 2013. *MATLAB User Manual,* The Math Works Inc., MA, USA, 282 pp.

NGA, 2014. National Geospatial-Intelligence Agency. Available at: http://msi.nga.mil/NGAPortal/MSI.portal (last accessed 30 May 2014).

NASA, 2013. Earthquake Births New Island off Pakistan. Available at: http://earthobservatory.nasa.gov/IOTD/view.php?id=82146 (last accessed 12 November 2013).

Okada, Y., 1985. Surface deformation due to shear and tensile faults in a half-space, *Bull. seism. Soc. Am.,* **75**(4), 1135–1154.

Pendse, C.G., 1946. The Mekran earthquake of the 28th November 1945, *India Meteorol. Depart. Sci. Notes,* **10**(125), 141–145.

Rabinovich, A.B., 1997. Spectral analysis of tsunami waves: separation of source and topography effects, *J. geophys. Res.,* **102**(12), 663–676.

Rabinovich, A.B., 2009. Seiches and harbour oscillations, in *Handbook of Coastal and Ocean Engineering,* pp. 193–236, ed. Kim, Y.C., World Scientific.

Satake, K., 1988. Effects of bathymetry on tsunami propagation: application of ray tracing to tsunamis, *Pure appl. Geophys.,* **126**(1), 27–36.

Satake, K., 2007. Volcanic origin of the 1741 Oshima-Oshima tsunami in the Japan Sea, *Earth Planets Space,* **59**(5), 381–390.

Satake, K., 2012. Tsunamis generated by submarine landslides, in *Submarine Mass Movements and Their Consequences,* pp. 475–484, eds Yamada, Y. *et al.*, Springer.

Satake, K. & Tanioka, Y., 2003. The July 1998 Papua New Guinea earthquake: mechanism and quantification of unusual tsunami generation, *Pure appl. Geophys.,* **160**(10–11), 2087–2118.

Schlüter, H.U., Prexl, A., Gaedicke, C., Roeser, H., Reichert, C., Meyer, H. & Von Daniels, C., 2002. The Makran accretionary wedge: sediment thicknesses and ages and the origin of mud volcanoes, *Mar. Geol.,* **185**(3), 219–232.

Sondhi, V.P., 1947. The Makran earthquake, 28th November 1945 – the birth of new islands, *Geol. Surv. Indian Miner.,* **1**(3), 147–157.

Synolakis, C.E., Bardet, J.P., Borrero, J.C., Davies, H.L., Okal, E.A., Silver, E.A., Sweet, S. & Tappin, D.R., 2002. The slump origin of the 1998 Papua New Guinea tsunami, *Proc. R. Soc. Lond., A.,* **458**(2020), 763–789.

Tanioka, Y. & Satake, K., 1996. Tsunami generation by horizontal displacement of ocean bottom, *Geophys. Res. Lett.,* **23**(8), 861–864.

Torrence, C. & Compo, G., 1998. A practical guide to wavelet analysis, *Bull. Am. Meteorol. Soc.,* **79,** 61–78.

USGS, 2013a. M7.7 - 61 km NNE of Awaran, Pakistan (BETA). Available at: http://comcat.cr.usgs.gov/earthquakes/eventpage/usb000jyiv#summary (last accessed 12 November 2013).

USGS, 2013b. National Earthquake Information Center (NEIC), earthquake catalog search. Available at: http://earthquake.usgs.gov/earthquakes/search/ (last accessed 15 December 2013).

USGS, 2013c. Preliminary finite fault results for the Sep 24, 2013 Mw 7.8 69 km NNE of Awaran, Pakistan Earthquake (Version 1). Available at: http://comcat.cr.usgs.gov/earthquakes/eventpage/usb000jyiv#scientific_finite-fault (last accessed 25 March 2014).

Wang, X., 2009. User manual for COMCOT version 1.7, first draft. Cornell University, 59 pp.

Watts, P., Borrero, J.C., Tappin, D.R., Bardet, J.P., Grilli, S.T. & Synolakis, C.E., 1999. Novel simulation technique employed on the 1998 Papua New Guinea tsunami, in *Proceedings of 22nd General Assembly IUGG,* 18–30 July, Birmingham, UK.

Watts, Ph., Grilli, S.T., Tappin, D. & Fryer, G.J., 2005. Tsunami generation by submarine mass failure. II: predictive equations and case studies, *J. Waterway Port Coast. Ocean Eng.,* **131**(6), 298–310.

Watts, Ph., Grilli, S.T., Kirby, J.T., Fryer, G.J & Tappin, D.R., 2003. Landslide tsunami case studies using a Boussinesq model and a fully nonlinear tsunami generation model, *Nat. Hazards Earth Syst. Sci.,* **3**(5), 391–402.

Wessel, P. & Smith, W.H.F., 1991. Free software helps map and display data, *EOS, Trans. Am. geophys. Un.,* **72,** 441 and 445–446.

Wiedicke, M., Neben, S. & Spiess, V., 2001. Mud volcanoes at the front of the Makran accretionary complex, Pakistan, *Mar. Geol.,* **172**(1), 57–73.